Superconductor
Science and
Technology

PAPER • **OPEN ACCESS**

Local structure analysis of 300 keV He^+ irradiated REBCO coated conductor using polarisation dependent Cu K edge EXAFS

To cite this article: Jarrod C Lewis *et al* 2025 *Supercond. Sci. Technol.* **38** 015022

OPEN ACCESS
IOP Publishing
Superconductor Science and Technology
Supercond. Sci. Technol. **38** (2025) 015022 (14pp)
https://doi.org/10.1088/1361-6668/ad9862

Local structure analysis of 300 keV He^+ irradiated REBCO coated conductor using polarisation dependent Cu K edge EXAFS

Jarrod C Lewis[1,2,*], Kirk Adams[1], William Iliffe[1,3], Matteo Aramini[2], Chris R M Grovenor[1], Rebecca J Nicholls[1], Sofia Diaz-Moreno[2] and Susannah C Speller[1]

[1] Materials Department, University of Oxford, Parks Road, Oxford OX1 3PH, United Kingdom
[2] Diamond Light Source, Harwell Science and Innovation Campus, Didcot OX11 0DE, United Kingdom
[3] Culham Centre for Fusion Energy, Culham Science Centre, Abingdon OX14 3EB, United Kingdom

E-mail: jarrod.lewis@materials.ox.ac.uk

Received 12 August 2024, revised 8 November 2024
Accepted for publication 28 November 2024
Published 20 December 2024

Abstract

Understanding irradiation damage of REBCO is increasingly of interest for compact tokamak fusion reactor designs, as these materials are critical for the proposed magnetic plasma confinement systems. Here commercially sourced samples of REBCO coated conductor are irradiated with 300 keV He^+ ions to a damage level of 169×10^{-3} displacements-per-atom, to the point where superconductivity is no longer detectable, meaning these samples correspond to a non-functional end-of-life component in a fusion reactor context. Subsequent analysis of the crystal structure through a combination of x-ray diffraction and x-ray absorption spectroscopy measurements reveals a complex variation away from the as-grown structure. The local structure probed by the spectroscopy measurements is further observed to change as a function of the relative polarisation of the incident x-ray beam, indicating that within this damage regime the structural anisotropy of the REBCO unit cell plays a determining role in where defects accumulate within the material. Here the local structure measurements probing the *a*-*b* plane of the system vary significantly less than those probing the *c*-axis direction following irradiation, mirroring the observed trend in the x-ray diffraction data that the *a:b* ratio is preserved upon irradiation whilst the absolute values increase, whereas the *c*-axis parameter expands. These observations highlight the role of oxygen defect formation in driving the degradation of superconductivity within irradiated REBCO. These changes are observed to preferentially accumulate along the *c*-axis of the material, indicating a possible mechanistic signature of the degradation of the superconducting properties within these systems that are evident using a local structure probe such as extended x-ray absorption fine structure.

* Author to whom any correspondence should be addressed.

Supplementary material for this article is available online

Keywords: REBCO, coated conductor, XAS, EXAFS, local structure, irradiation damage, Frenkel defect

1. Introduction

The next generation of small-scale tokamak designs are reliant upon high-temperature superconductor (HTS) coil technologies for the confinement of the plasma in which the fusion process occurs [1, 2]. A leading HTS candidate material for these coils are the rare-earth barium cuprates (REBCO), (RE)$Ba_2Cu_3O_{7-\delta}$, which are commercially available as flexible tapes of micron thick pseudo-single crystal thin films produced in a coated conductor architecture [3]. Within these applications, the conditions in which these HTS coils are situated exposes the material to a flux of high energy neutrons. Prolonged neutron irradiation is associated with an eventual degradation of the superconducting properties of REBCO, after an initial increase in in-field performance due to an enhanced density of flux pinning centres from the formation of point defects and damage cascades within the crystal structure [4]. Eventually this accumulation of irradiation damage within the HTS can result in the complete loss of superconductivity, which would introduce a finite component lifetime for REBCO coils within a tokamak [5–10].

The defect morphologies formed within REBCO by particle irradiation are non-trivial [11], in part due to the complexity of the pristine crystal structure. REBCO coated conductors are biaxially textured, with the *c*-axis of the crystal aligned to the surface normal, and the *a*/*b* axes aligned parallel to the length of the material. Fully oxygenated REBCO has an orthorhombic structure, in which the copper atoms have two coordination environments, Cu(1) and Cu(2). These environments are typically described as Cu(1) chain and Cu(2) planes, with these different Cu environments labelled in figure 1.

This crystal structure is further complicated by the fact that REBCO materials are naturally twinned, with <110> twin boundaries and domains rotated 90° about the *c*-axis. This results in bulk probes of material structure, such as x-ray diffraction and x-ray absorption spectroscopy, sampling both the *a* and *b* directions of the material simultaneously. Furthermore, stacking faults are noted to occur which introduce a minority of additional Cu local environments to the system, in the form of (RE)$Ba_2Cu_4O_8$ intergrowths [12]. We would expect both REBCO phases will be affected by irradiation damage, and thus the initial stacking fault density will impact the observed alteration to both the superconducting properties and arrangement of atoms within the material structure following irradiation.

Building upon previous work to understand the impact of irradiation on the superconducting properties of REBCO and the characteristics of the irradiation induced defects within these systems [9, 10, 13, 14], further measurements of the local coordination environment of the copper atoms are undertaken. Here the Cu K-edge is measured using x-ray absorption spectroscopy (XAS), with these measurements extended to higher energies above the absorption edge to capture the extended x-ray absorption fine structure (EXAFS) within the XAS signal. This technique provides an element specific probe of the local structure of a material for a given absorbing atomic species, and thus provides information on the inter atomic distances between the absorbing Cu atoms and their neighbouring atomic sites. The short-order structural information obtained by the EXAFS analysis complements previous studies of the electronic structure of REBCO under irradiation [13, 14], and provides an additional verification of the validity of the defect structures modelled using Density Functional Theory.

Furthermore by collecting measurements as a function of polarisation, the inter atomic distances probed by this technique can be preferentially tuned to be sensitive to either the *c*-axis or *a*-*b* oriented components of the REBCO structure. In this measurement mode, the individual scattering paths have a relative amplitude factor that is dependent on both the incident angle of the oscillating electromagnetic field of the x-rays upon the sample, and the relative angle of the scattering path relative to the absorbing atom. Schematically this is shown in figure 2 where each angle is defined explicitly, with the polarised amplitude factors, χ_{pol}, being calculable relative to the 45° absorption spectrum [15], χ_{45}, as

$$\chi_{\mathrm{pol}} = 3(\sin(\theta_E) \times \sin(\theta_A) \times \cos(\phi_E - \phi_A) + \cos(\theta_E) \times \cos(\theta_A))^2 \chi_{45}. \quad (1)$$

Using equation (1), these calculations enable the different scattering paths to be probed preferentially, by collecting measurements with the sample oriented such that the beam is incident at 80° (aligned to the *c*-axis) and 10° (aligned to the *a*-*b* plane) relative to the sample surface normal.

To study the impact of irradiation on the REBCO unit cell, He^+ ions are used as a proxy irradiation species for high energy neutrons that are the predominant irradiation species within fusion reactor applications. This is based on previous work that suggests a similarity between point defects induced by He ion irradiation and neutron irradiation [14], and so here are employed to study the underlying mechanisms of the degradation of superconductivity through the accumulation of point defects. Although it is non-trivial to relate ion and neutron damage profiles for a given fluence in a quantitative manner due to neutron irradiation being dependent on both the neutron energy and the diverse variety of possible nuclear reactions, the ion irradiation treatment employed in this study corresponds to damage levels well beyond the operational lifetime

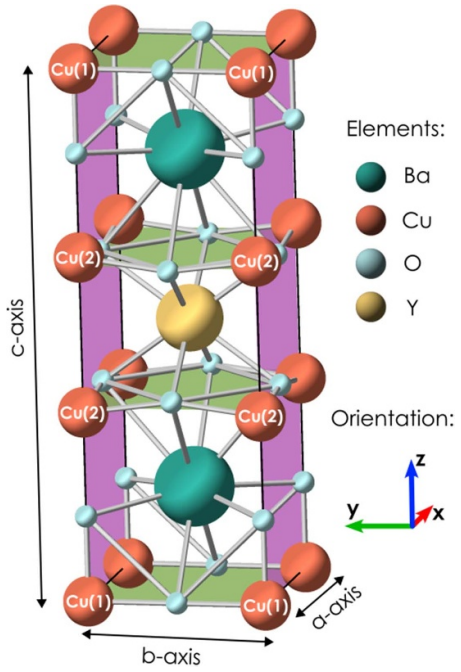

Figure 1. The REBCO unit cell, shown with Y at the RE site. Labelled are the individual elements within the orthorhombic structure, as well as the directions corresponding to the *c*-axis (shaded magenta) and the *a*-*b* planes (shaded green). Each of the two Cu environments are labelled for the front face of the unit cell.

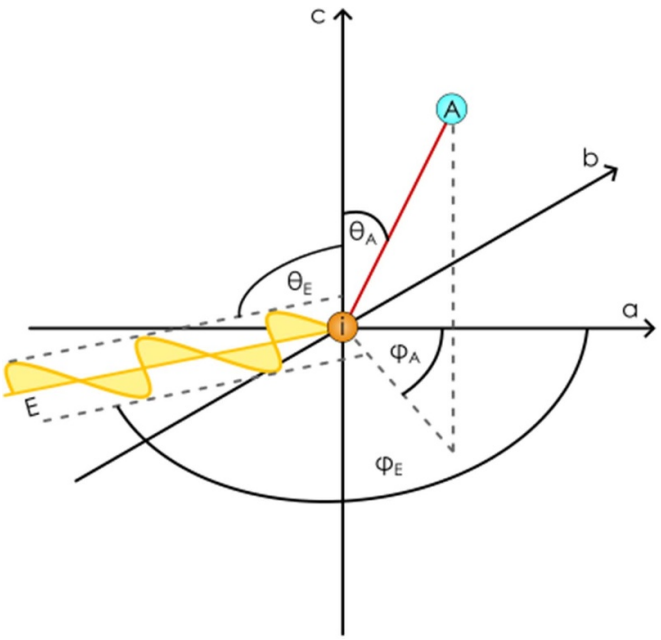

Figure 2. Polarised x-ray absorption schematic for an absorbing atom i, with the incident x-ray shown as a sinusoidal oscillation of the electromagnetic field relative to the axes of a crystal unit cell. Here the angles relative to the field are subscript E, with subscript A denoting angles relative to the scattering atom A.

of a REBCO fusion component. As such, this treatment simulates the damage that would correspond to a loss of superconductivity in the REBCO layer to probe the underlying mechanisms, rather than a simulation of the *in-situ* irradiation expected during routine operation.

In addition to the XAS studies, x-ray diffraction (XRD) was also used to determine the structural impact of irradiation on REBCO. This technique was used to probe the static crystal structure of the material, and complement the information obtained from the XAS analysis. To relate these probes to the superconductivity of the irradiated system, the superconducting transition temperature was characterised using vibrating sample magnetometry (VSM). Through this combination of methods, the impact of irradiation on the local structure of Cu in REBCO is evaluated, providing new insights into the mechanisms that drive the loss of superconductivity within this operational regime of HTS materials relevant to applications in emerging technologies.

2. Methods

2.1. Sample properties and processing

The REBCO coated conductor samples studied herein were sourced from SuperPower, from a batch produced in 2011. Here the rare earth element site is partially occupied by both Y and Gd in a 1:1 volume ratio, producing an overall (Y/Gd)$Ba_2Cu_3O_{7-\delta}$ unit cell. The superconducting properties of this system are improved by the inclusion of $BaZrO_3$ nanorods which improve the superconducting current density through acting as artificial pinning centres. As manufactured, these coated conductor samples are encased in protective capping layers of Ag (2 μm) and Cu (20 μm), with the REBCO layer (1 μm) grown by MOVCD on top of a series of buffer materials that sit between the REBCO and a C276 Hastelloy substrate (50 μm). Starting at the REBCO layer and terminating next to the Hastelloy substrate, the buffer layer sequence for these coated conductors is AlO_3, Y_2O_3, ion-beam assisted deposited MgO, and $LaMnO_3$.

Prior to characterisation, the outermost 20 μm Cu and 2 μm Ag capping layers were etched away using $FeCl_3$ solution (60 g $FeCl_3$ to 100 ml water) to remove the Cu, followed by a mixture of ammonia and hydrogen peroxide (each 30% water solutions mixed in a 1:1 ratio) to remove the resulting AgCl reaction product and the Ag layer. This process exposed the surface of the 1 μm thick MOCVD deposited REBCO layer. The samples were then punched from the as-produced 4 mm wide tape into a 3 mm diameter disc.

2.2. Ion irradiation

Ion irradiation was carried out at the Surrey Ion Beam Centre using 300 keV He^+ ions incident onto the coated conductor sample to a fluence of 1.6×10^{16} cm^{-2}, with a beam current of 130 nA. The impact of this irradiation was analysed using SRIM [16], where a full cascade calculation was carried out using elemental threshold displacement energies (E_d) of $E_d(Gd) = E_d(Y) = E_d(Ba) = E_d(O) = E_d(Ni) = 25$ eV, and $E_d(Cu) = 40$ eV [17], and lattice binding and surface binding energies set to 0 eV. The number of ions simulated was 1×10^5, with the mass density of the REBCO taken to be

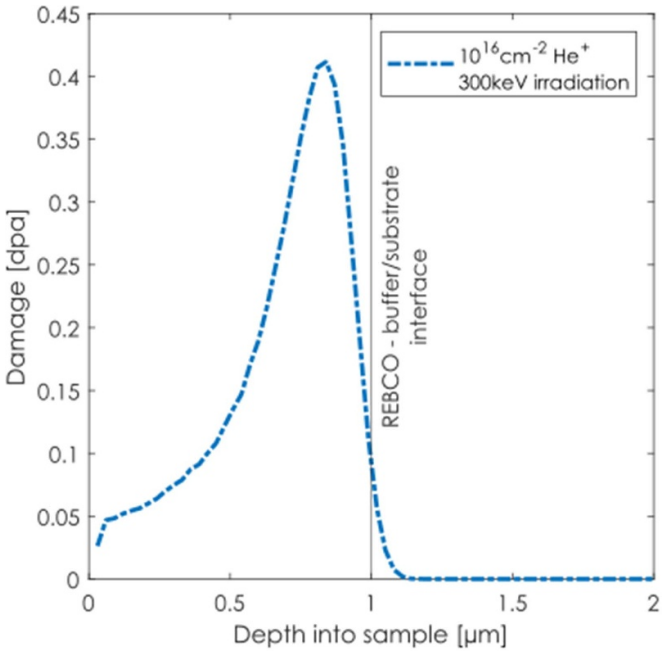

Figure 3. Simulated ion implantation profile for He^+ into REBCO, calculated using SRIM. The interface between the REBCO layer and the underlying buffer and substrate materials is shown by a solid black line, with the irradiation profile (blue dashed line) corresponding to an average damage level of 169 mdpa.

6.632 gcm^{-3}. Here the Hastelloy C276 substrate was modelled as pure Ni of density 8.895 gcm^{-3}, and the intervening buffer layers were omitted. This simulation resulted in an average displacement per atom (dpa) damage level of 169 mdpa, with the damage profile shown in figure 3.

Here it is evident that the Bragg peak of the incident radiation is situated within the 1 μm thick REBCO layer of the coated conductor, and not in the buffer layers or substrate. This results in a non-uniform irradiation profile throughout the REBCO layer.

2.3. X-ray diffraction measurements

XRD characterisation was carried out using a Cu Kα source in a Panalytical Empyrean diffractometer configured in Bragg–Brentano geometry, with a 3-axis (z-χ-Φ) cradle sample mount. Highscore$^+$ software was used to fit the background and the diffraction peak centres, and to strip the Kα_2 component of the data. The c-lattice parameter was calculated from these peak centres using the Nelson-Riley function, where the lattice parameter was the extrapolated y-intercept, accounting for the systematic errors from mounting the sample. The in-plane a-b lattice parameters were calculated from off-specular, in-plane measurements collected using the reciprocal space mapping function of the diffractometer. Here the finite angular range of the diffractometer limited the number of reachable reflections, resulting in a larger uncertainty in the a/b axis lattice parameter values calculated.

2.4. X-ray absorption measurements

Room temperature XAS measurements were collected at the Diamond Light Source (Didcot, UK), beamline I20-Scanning. The synchrotron ring energy was 3 GeV at a current of 300 mA, and the beamline made use of a bespoke four-bounce scanning Si(111) monochromator with higher harmonics rejected through the use of two Rh-coated mirrors at 5 mrad incidence angle. X-rays were detected via a 64-element monolithic Ge detector coupled with Xspress4 readout system [18], and the energy of the monochromatic beam was calibrated by using the first derivative of the XAS spectrum of a Cu foil measured in transmission.

Measurements were collected with each 3 mm diameter sample mounted onto a Teflon disc with double sided adhesive tape, held in place within a plastic holder. This setup ensured that there was no Cu present within the mounting apparatus, which would mask the Cu K-edge absorption signal from the sample. The sample stage was adjustable in x-y-z and rotation around the azimuthal angle, enabling alignment of the sample to the beam and polarisation dependent measurements to be achieved.

All XAS data normalisation was carried out using standard processing procedures in the Demeter analysis suite [19], with multiple-scattering path fitting achieved using a pristine $YBa_2Cu_3O_7$ unit cell reference file (ICSD-62465) [20] as a basis for scattering path calculations. To minimise the parameter space, all fits were based on the pristine structure, with a full list of both the fitted and constrained parameters included in the supplementary information as tables SI table 1—SI table 3. Notably, the pristine structure includes a scattering path along the c-axis that is similar in distance to one from interstitial O in the Frenkel defect structure, which informs the evaluation of the XAS fits.

2.5. Simulated spectra using FEFF10

EXAFS spectra were simulated for the $REBa_2Cu_3O_{7-\delta}$ Frenkel defect and $REBa_2Cu_4O_8$ (REBCO-124) stacking fault defect using FEFF10 [21, 22]. Here the Frenkel defect structure is formed by moving an O atom at an O2 site of pristine REBCO-123, in the a-b plane between neighbouring Cu(2) atoms, to an interstitial position between two neighbouring Cu(2) atoms along the c-axis direction [13], introducing new Cu-O distances to the unit cell. Two Frenkel model defect structures were used: the $1 \times 1 \times 1$ defect structure from [13] and a $2 \times 2 \times 1$ supercell which was created based on a $2 \times 2 \times 1$ supercell of the REBCO-123 structure with one Frenkel defect in it. The geometry of the $2 \times 2 \times 1$ supercell structure was optimised using the DFT code CASTEP [23], with the rSCAN functional and ultrasoft pseudopotentials. The structures were constrained so that angles α, β and γ remained equal to 90°. A cut-off energy of 650 eV, k-point spacing of 0.03 Å^{-1} and fine grid scale value (which determines the size of the fine grid relative to the cut-off sphere) of 2.5 were used and the structure were optimised until the forces on atoms

were less than 5×10^{-3} eV Å^{-1}. This is the same procedure that was used in [13] to geometry optimised the $1 \times 1 \times 1$ Frenkel defect. The unit cell is shown for the $1 \times 1 \times 1$ model in the supplementary information as SI figure 1. It is worth noting that the geometry optimised Frenkel defect unit cells have slightly different c-axis lattice parameters following geometry optimisation with the previously reported $1 \times 1 \times 1$ cell having $c = 12.20$ Å [13] and the $2 \times 2 \times 1$ case having $c = 11.69$ Å. This variation informed the qualitative comparison of the simulated spectra rather than using these structures for quantitative fits to the experimental data.

The REBCO-124 calculations made use of ICSD-74259 as a reference structure [24], shown in SI figure 2. Here each simulation approximates the rare-earth site to be occupied solely by Y, as previous studied have shown that there is little spectroscopic difference between the local structure of either Gd or Y rare-earth sites within REBCO [13, 14].

In FEFF10, each spectrum was simulated for the Cu K-edge with a converged self-consistent potential of radius of 5.0 Å to a spectral range of $k = 20$ Å^{-1}. The longest path simulated was fixed to 5 Å, and the amplitude factor $S_0{}^2$ was set to unity. The Debye–Waller factors of the EXAFS were calculated for a sample temperature of 300 K and a Debye–Waller temperature of 400 K, with this value determined through a review of published ambient pressure values for $YBa_2Cu_3O_{7-\delta}$ [25–31].

To enable a qualitative comparison between the REBCO coated conductor experimental spectra and these defect model simulations, the simulated spectra had their E_0 values of the simulated spectra were set to the relevant experimental value for the pristine sample, which for the 45° spectra was $E_0 = 8990.3$ eV.

2.6. Vibrating sample magnetometry measurements

Critical temperature (T_c) values were determined using a Quantum Design Magnetic Property Measurement System (MPMS 3) in Vibrating Sample Magnetometer mode. Secured within a brass holder by two quartz cylinders and polyimide tape, each sample disc was zero-field cooled to 10 K before a 5 mT field was applied.

The magnetic moment of each sample was then recorded as a function of temperature during warming to 120 K, with T_c onset defined as the point of divergence from a linear fit of the normal-state moment.

3. Results

3.1. X-ray diffraction

The crystal structure of the coated conductor HTS REBCO layer was characterised using XRD, with the standard phase identification θ-2θ scan plotted in figure 4 for both the pristine sample and after irradiation. Here it is evident in the pristine (blue) pattern that the diffraction peaks are sharp and well defined relative to the background, indicating a good degree of crystallinity. (00l) reflections were clearly observable up to the (0013) peak at $2\theta = 117.38°$, enabling for an accurate calculation of the c-axis lattice parameter of the sample.

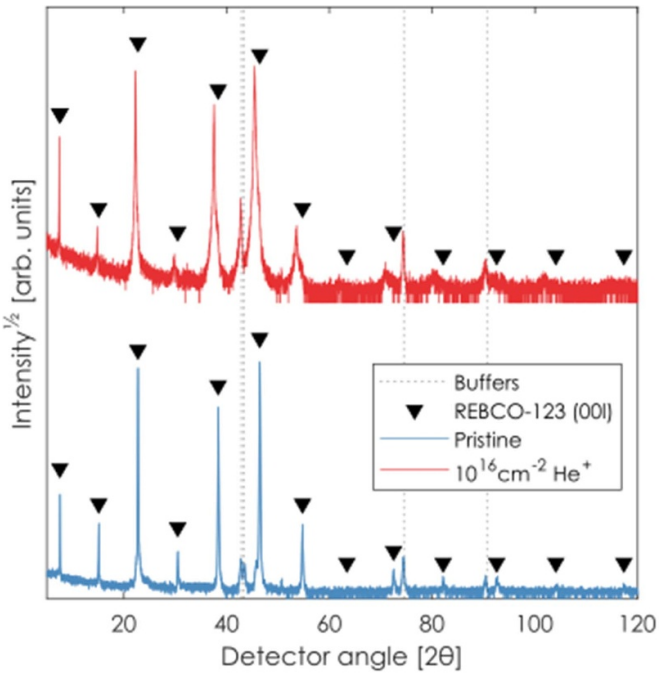

Figure 4. XRD patterns of the REBCO coated conductor when pristine (blue) and following He^+ irradiation (red). Peaks attributed to the buffer layer materials are shown with dashed black lines, with the remaining peaks identified as REBCO (00l) peaks. Reference (00l) peaks for pristine bulk REBCO are included as black triangles relative to both diffraction patterns to highlight their relative agreement.

Upon irradiation, the XRD pattern (red) becomes broader in 2θ, indicating a greater degree of disorder within the interplanar distances of the crystal, in keeping with the inhomogeneous irradiation profile of figure 3. It is notable however that no additional phases emerge as a function of the irradiation treatment. The relatively higher background signal and decreased relative signal amplitude of the diffraction peaks further indicate an increase in disorder within the static crystal structure upon irradiation.

In-plane measurements of the REBCO crystal structure are plotted in figure 5, with the pristine (309) reflection plotted in figure 5(A), and the same reflection plotted after He^+ irradiation in figure 5(B). In the pristine scan, the twinning of the REBCO crystal structure is clear, with two reflections separated in 2θ clearly visible. Here the left peak corresponds to the (039), with the right-hand peak at larger 2θ corresponding to the twinned (309) reflection. Both reflections are pronounced relative to the background of the measurement. Upon irradiation, the data of figure 5(B) shows both a heightened background level and a loss of the two distinct peaks from the (309) and (039) reflections. This is further shown in the line scans across the maxima of these plots, included in the supplementary information as SI figure 3. These changes to the in-plane reflections demonstrate that the irradiation damage not only

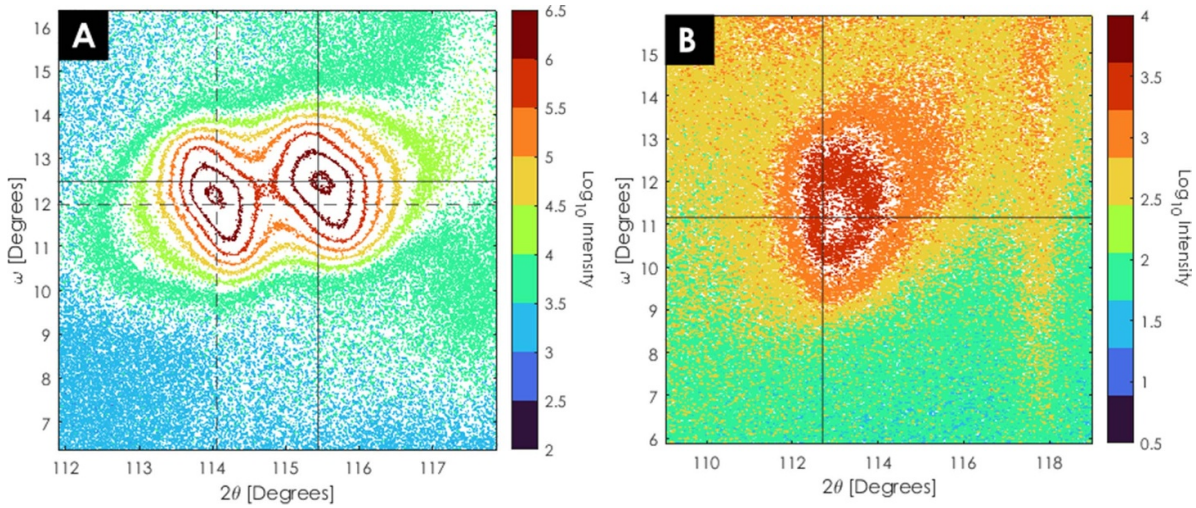

Figure 5. Off-specular XRD patterns, scanned in ω-2θ over the (309) reflection. (A) Pristine REBCO, (B) He^+ irradiated REBCO. (A) Clearly displays the characteristic twinning associated with high quality crystalline REBCO, which is then lost in (B) upon irradiation. Peak maxima for each plot are denoted as the intersection of the black lines.

Table 1. Lattice parameters determined by XRD analysis for each coated conductor sample as a function of sample treatment.

Sample	*a*-axis [Å]	*b*-axis [Å]	*c*-axis [Å]	((a + b)/2)/c	*a*-axis % shift	*b*-axis % shift	*c*-axis % shift
Pristine	3.822 ± 0.001	3.868 ± 0.020	11.727 ± 0.003	0.328	0.99	0.98	1.82
10^{16} He^+	3.860 ± 0.020	3.906 ± 0.050	11.941 ± 0.010	0.325			

results in an alteration of the *c*-axis lattice parameter noted in figure 4, but also impacts the in-plane *a*-axis and *b*-axis lattice parameters.

Using the data plotted in figures 4 and 5, and additional in-plane scans included in the supplementary information as SI figure 4 (with the corresponding line scans shown as SI figure 5), the lattice parameters of the REBCO layer tabulated in table 1. These were calculated using the 2θ corresponding to the maximum peak intensities highlighted on each figure with the intersecting lines. Table 1 shows that all three lattice parameters increase upon irradiation, with the *c*-axis lattice parameter increasing the most with approximately a factor of 2 greater percentage change observed along the *c*-axis of the unit cell relative to the *a*-axis and *b*-axis. Both the out-of-pane and in-plane measurements of figures 4 and 5 display less well defined peaks upon irradiation which are broader in 2θ, further indicating a degradation in crystal quality following this treatment, suggesting an increase of disorder within the sample. It is however notable that the *a:b* lattice parameter ratio is retained upon irradiation, with no indication from this XRD analysis that either of these in-plane axes are more susceptible to the impact of the irradiation treatment than the other.

Furthermore, table 1 highlights that despite the observed increase in disorder upon irradiation, the XRD characterisation does not provide evidence for a loss of the orthorhombic crystal structure following irradiation. As the orthorhombic to tetragonal phase transition is strongly associated with the loss of O from the REBCO structure, this instead supports the retention of oxygenation of the material, with O instead being displaced within the material by the incident irradiation.

3.2. Superconducting transition temperature measurements

Magnetic characterisation of the superconducting transition temperature was performed using a VSM, with the results for these REBCO samples plotted in figure 6. Here it is evident that the pristine sample displayed a superconducting transition with an onset $T_c = 89.4$ K, but the irradiated sample did not undergo a superconducting transition above 10 K. This indicates a significant suppression in the superconducting properties of the coated conductor REBCO layer, in agreement with previously reported measurements [13].

3.3. EXAFS

The effect of the sample treatment on the local disorder in the REBCO unit cell has been analysed using EXAFS measurements as a local probe of disorder within the REBCO unit cell. For quantitative analysis, the fits are constrained based on experimental lattice parameters measured by XRD and the relative positions of atoms within the unit cell. For example, the Cu(1) to O nearest-neighbour path along the *b*-axis of figure 1 is constrained to have the O site half way between the two neighbouring Cu(1) sites. The different scattering path lengths associated with each Cu environment in pristine REBCO are shown in figure 7 as the Fourier transform modulus, with the relative distance to each scattering atom is shown in decimal notation in figures 7(A) and (B), such that O1.1 is the first nearest O at an O1 site, with O1.2 being the second nearest.

Due to the high number of similar scattering distances from the REBCO Cu sites, it follows that the constructive

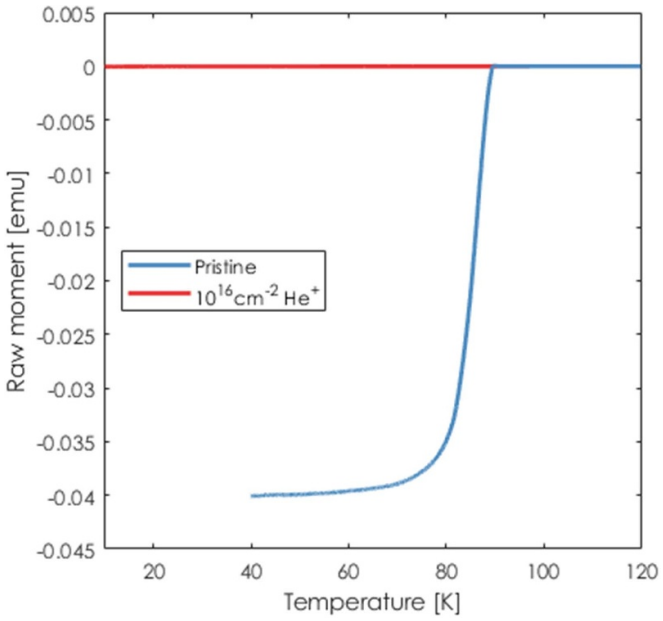

Figure 6. T_c measurements of the REBCO coated conductors before and after He^+ irradiation. Here the superconducting transition for the irradiated sample is not visible, thus $T_c < 10$ K.

and destructive interference of signals from these scattering paths results in a complex EXAFS spectrum, sensitive to both subtle changes to the unit cell and sufficiently complex to make the determination of the origin of a given spectral change challenging. This can be clearly demonstrated in the Cu-O single scattering paths, colloquially referred to as the first oxygen shell, which when plotted in terms of the wavenumber k (figure 8) show how paths with similar inter atomic distances can produce destructive interference in k-space that would impact the Fourier transformed real space spectra. The Cu(1)-O1.1 path (blue, $R = 1.846$ Å) relative to Cu(2)-O1.1 (purple, $R = 2.296$ Å) is the clearest example of this.

With these details of the REBCO local structure established, the EXAFS analysis is approached in two phases. First, a quantitative fit is undertaken for the pristine coated conductor samples. The aim of this analysis is to establish how close the as-grown material is to the 'perfect' crystal structure, and whether any manufacturing defects are evident.

However, as the irradiation profile detailed in figure 3 is non-uniform, and as the information content of the REBCO unit cell is high when probed using this local structure methodology as there are many overlapping paths, only the first oxygen shell of paths (shown in figure 8) are quantitatively fitted in the irradiated sample. A more qualitative approach is used to interpret the longer paths. This enables the sensitivity of the nearest neighbour oxygen region of the spectra to be exploited, whilst also avoiding the complexity of modelling multiple scattering paths at higher inter atomic distances which would be highly sensitive to defects in the second nearest neighbour oxygen positions, and thus if quantitatively analysed would offer limited further insight.

For each data set, the complete EXAFS fitting parameters are detailed in the supplementary information as SI tables 1 and 2 for the pristine sample measured at angles of 10° and 80° respectively, and in SI table 3 for the He^+ irradiated sample. The pristine data are modelled between 1–4.5 Å for each measured angle including high-amplitude multiple scattering paths, whereas the irradiated analysis was limited to the first shell between 1–2.5 Å and thus only includes Cu-O single scattering paths. All subsequent Fourier transformed (FT) EXAFS signal plots are phase uncorrected, such that the plotted peaks are offset relative to their fitted inter atomic distances. For the 10° data, paths were constrained where possible to be in accordance with the XRD derived a-axis and b-axis lattice parameters to reduce to the parameter space of the fits, and to keep the model consistent with the static structure characterised by XRD in figures 4 and 5. The 45° data contain significant scattering amplitudes from both a/b plane and c-axis aligned paths, and so are presented unfitted to avoid overparameterisation. The 80° EXAFS inter atomic distance analysis is a fitted model where these inter atomic distances were allowed to vary, as these are oriented along the c-axis of the material. The decision to fit along the c-axis direction, rather than using the XRD determined c-axis lattice parameter values, is motivated by the finite information range probed by EXAFS being ≈5 Å, meaning that the c-axis lattice parameters determined in the analysis of figure 4 are of limited utility for fitting scattering paths that contribute towards the detected EXAFS signal. All fits are performed in R-space, with the respective k-range that was used for the FT of the data detailed in the supplementary information in the corresponding parameter table.

For the pristine sample, the FT of the measured spectra is plotted for each of the three measured angles in figure 9(A). Here it is evident that the spectra vary as a function of the measurement angle, as shown by equation (1), such that different paths have angle dependent magnitudes. Overall the spectral features of figure 9(A) agree well with the expected inter atomic distance distribution within pristine REBCO, highlighting the agreement between the static structure probed by XRD and this local structure probe.

This angular dependence then informs the fits for the 10° and 80° FT plotted in figures 9(B) and (C) respectively. The 10° data, which is more sensitive to the a-b plane, displays some disagreement in the FT peak around 3.7 Å with the remainder of the spectra being well captured by the pristine model, whereas the 80° data that is preferentially aligned along the c-axis of the unit cell shows less disagreement in this region. It is however notable that the first FT peak in the 80° data, corresponding to the Cu-O scattering from the nearest neighbour O sites is less well captured by the pristine model, indicating that the positions of the O atoms that occupy the site between the Cu(1) and Cu(2) sites along the c-axis of the unit cell are likely to be more variable than would be expected for a perfect single crystal of REBCO. Overall, the fitted spectra of figure 9 show a good level of agreement between the FT data and the model, indicating that the local structure of the as manufactured coated conductor is well approximated by the $YBa_2Cu_3O_{7-\delta}$ scattering path model.

The irradiation treatment however produces a marked evolution of the observed spectra, which are plotted relative to the

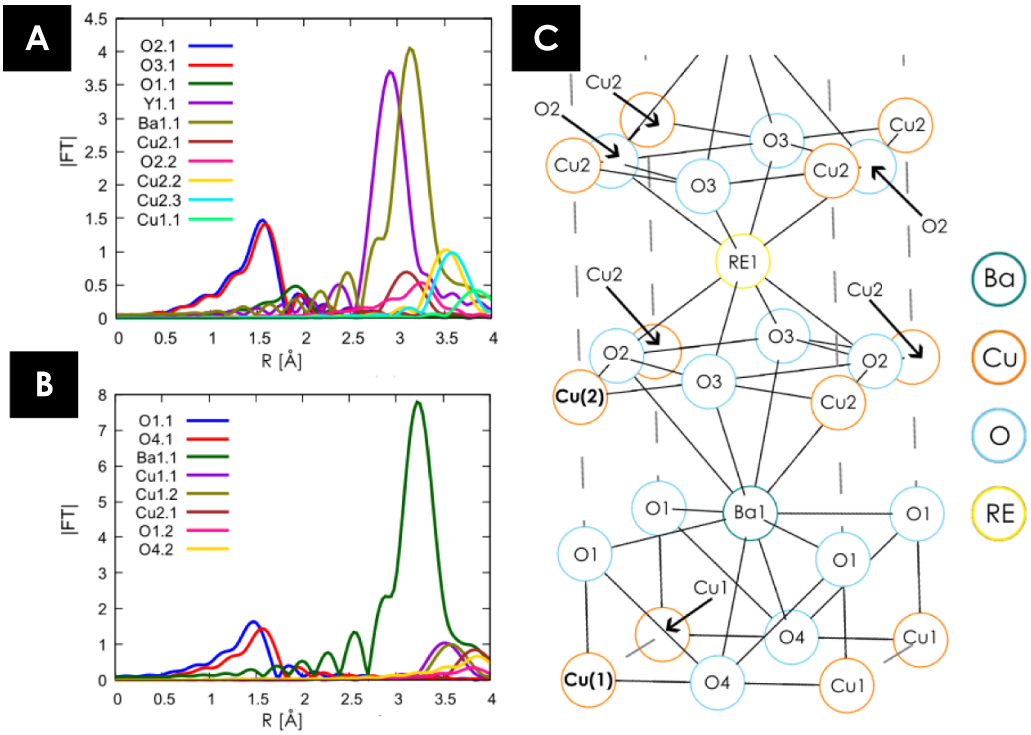

Figure 7. Single scattering paths of pristine REBCO plotted up to 4 Å, with this range avoiding the multiple scattering paths between 4.0–4.5 Å. Paths were calculated using FEFF with an initial REBCO input CIF file (ICSD-62465) [20]. (A) Cu(2) paths, (B) Cu(1) paths. (C) Diagram of the Cu environments of REBCO, with the scattering sites labelled and potential Cu absorber sites highlighted in bold. Here the boundary of the unit cell is shown by the dashed lines, with the bonds between atoms shown by the solid lines. The unit cell is truncated along the *c*-axis for clarity.

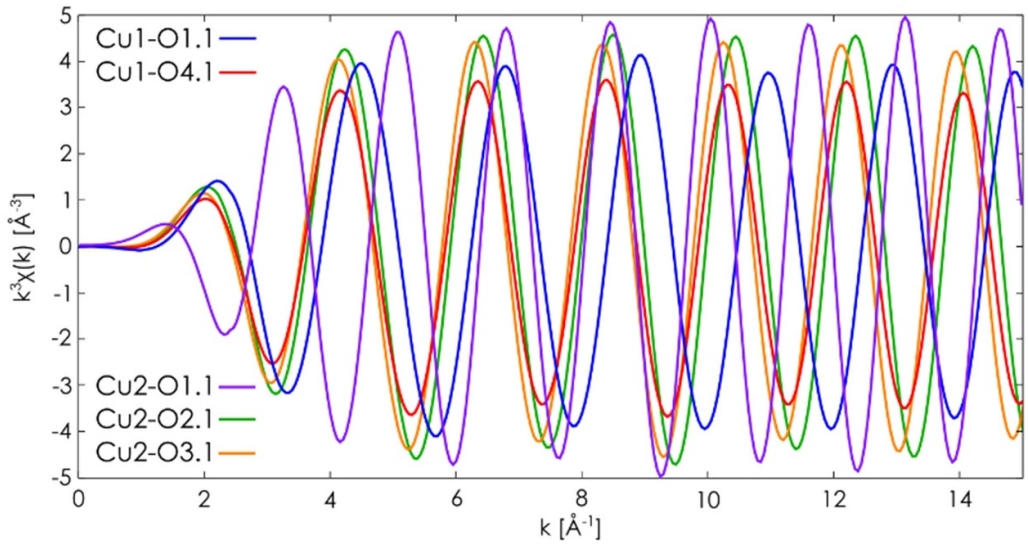

Figure 8. The single scattering Cu-O paths of REBCO, plotted for both REBCO Cu absorption environments for the nearest neighbour O sites ($R \leqslant 2.5$ Å) that make up the first coordination shell.

corresponding pristine FT spectra below in figure 10, again in terms of the absolute magnitude and real component of the Fourier transform. The extracted EXAFS signals are included in the supplementary information (SI figure 6) as *k*-dependent plots.

In the He^+ irradiated data (red), the amplitude of the 3–4 Å FT peaks in the 45° spectra of figure 10(A) decrease in keeping with the increased disorder seen in the XRD measurements of figure 5, whereas the FT peak at 1–2 Å remains largely unchanged with only a slight shift to lower inter atomic distance. This highlights the value of polarisation dependent methodologies for local structure probes of such complex materials, as it is challenging to gain further insight into the evolution of the local structure from this data set alone without

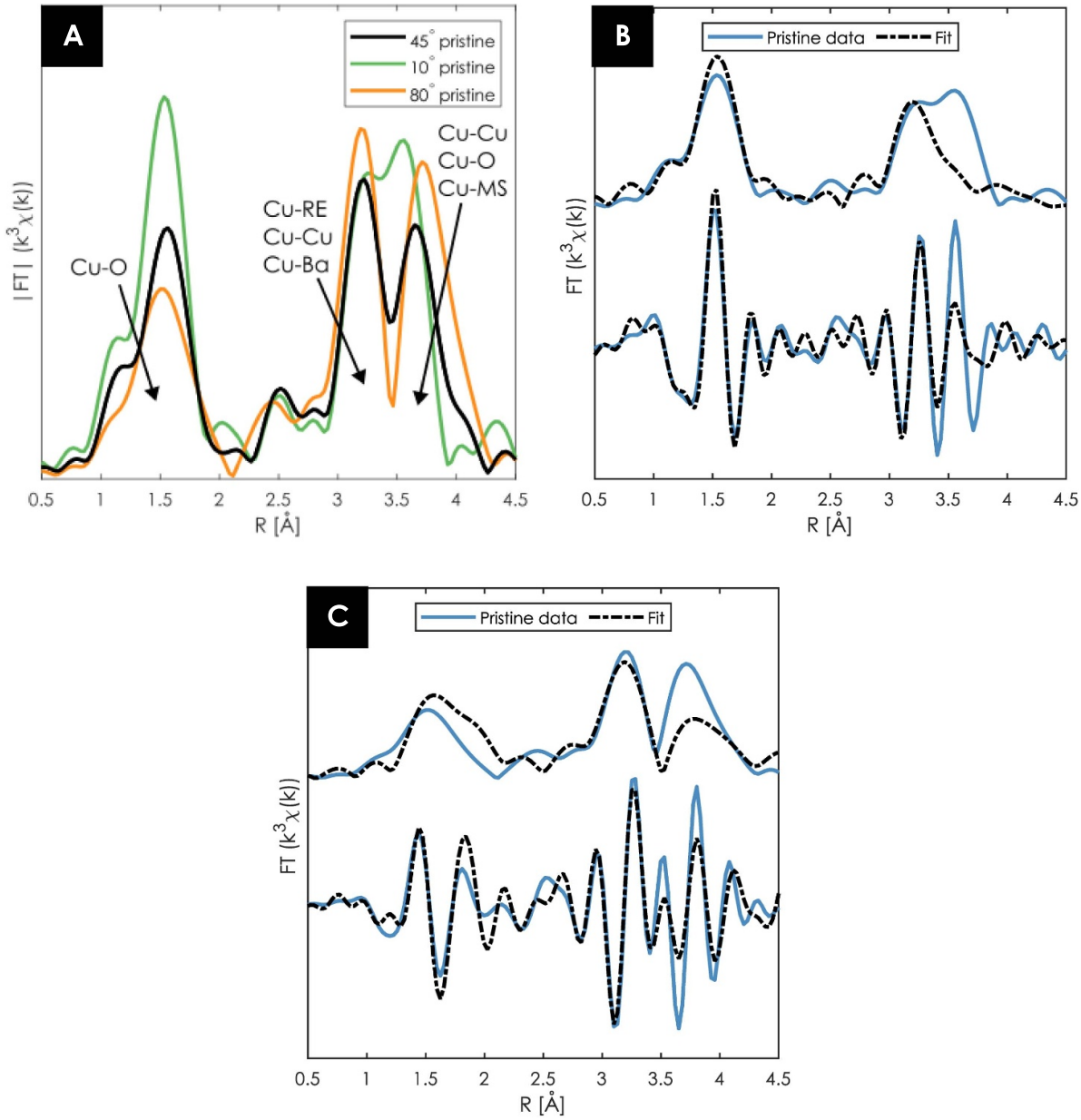

Figure 9. Analysis of pristine sample EXAFS. (A) The magnitude of the Fourier transforms at 45° (black), 10° (green), and 80° (orange), with the main features labelled. Here MS denotes multiple-scattering paths. The other panels show experimental data (blue solid lines) and the best fit (dashed lines) of the magnitude (upper) and real part (lower) of the Fourier transform of the pristine sample EXAFS: (B) 10°, and (C) 80° measurement angles. The FT of these signals utilised k-ranges of 3–13.15 $Å^{-1}$ (45°), 3–13.5 $Å^{-1}$ (10°), and 3–14 $Å^{-1}$ (80°).

comparison to polarised measurements that deconvolute the different FT spectral components.

In figure 10(B) the 10° He^{+} irradiated data (red) displays the same loss of amplitude in the 3–4 Å region as observed in the 45° FT data of figure 10(A), but a clearer distinction between the contributing peaks is more evident than in the pristine data (blue). The 1–2 Å FT peak also shifts slightly to lower inter atomic distance, but the main change to the spectra is again in the 3–4 Å region of the plot associated with the Cu-Cu, Cu-Ba, and Cu-RE scattering along with the second nearest neighbour Cu-O distances. This implies a small change to the *a-b* plane of the REBCO with the features centred at similar inter atomic distances, whereas the previously noted disorder observed by XRD continues to modulate the spectral amplitude with increasing distance from the absorbing Cu atom.

The 80° FT spectra, plotted in figure 10(C), are preferentially sampling the *c*-axis of the REBCO unit cell. Upon He^{+} irradiation, the data (red) continues the previously described trend in the lowering of the 3–4 Å FT peak amplitude, but here shows a sharper FT peak between 1–2 Å. As highlighted by figures 7 and 8, this indicates a movement of the O1.1 site that sits along the *c*-axis of the unit cell, resulting in the previously partially destructive superposition of the Cu-O1.1 scattering paths from Cu(1) and Cu(2) moving into phase, resulting in the observed increase in spectral amplitude within this region.

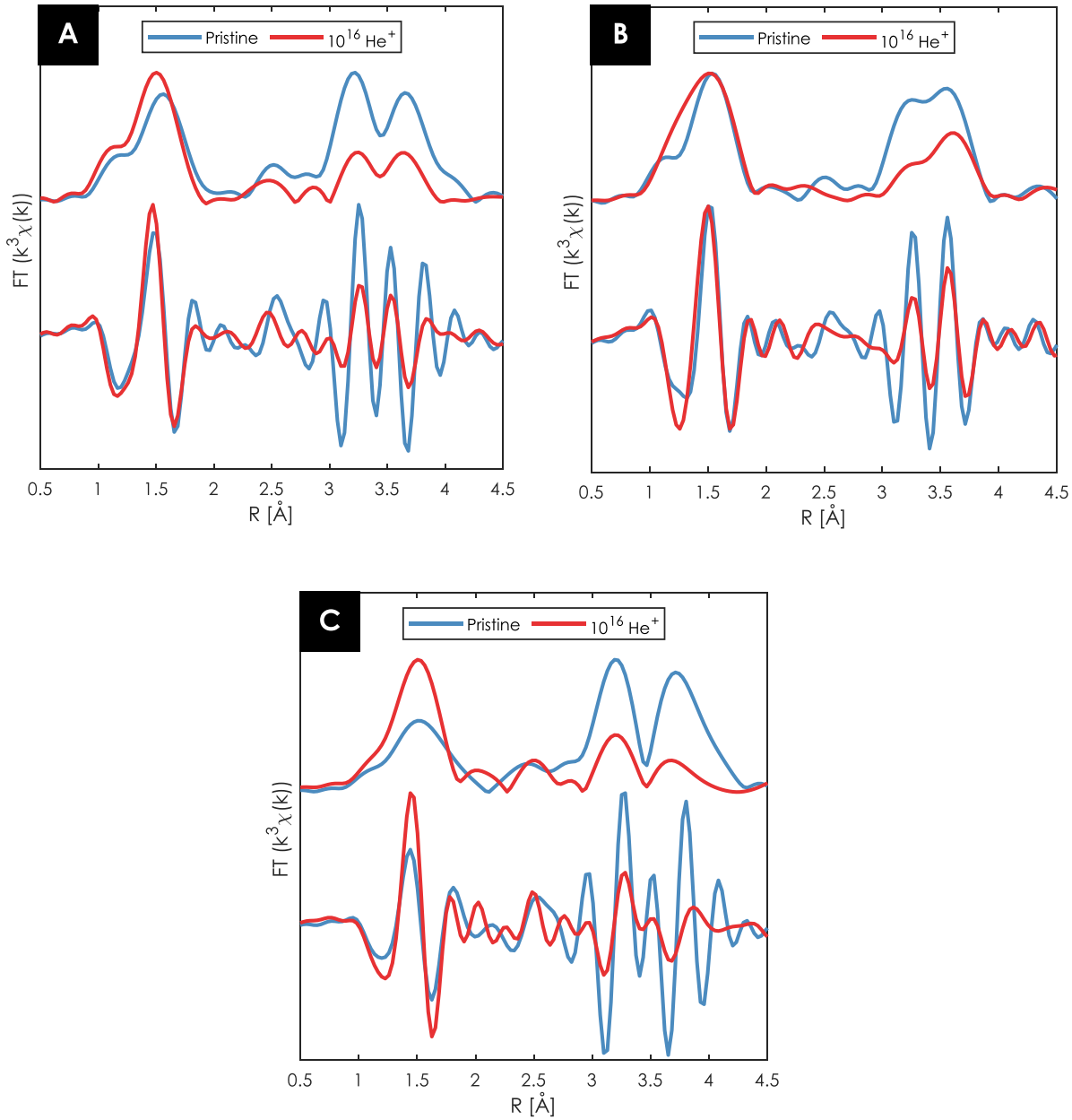

Figure 10. Experimental data for the pristine (blue) and irradiated (red) sample, plotted as the magnitude (upper) and real part (lower) of the Fourier transform: (A) 45°, (B) 10°, and (C) 80° measurement angles. The FT of these signals utilised a *k*-range for the pristine (blue) measurements of: (A) 3–13.15 Å^{-1}, (B) 3–13.5 Å^{-1}, (C) 3–14 Å^{-1}. The *k*-ranges used for the irradiated (red) measurements are: (A) 3–14 Å^{-1}, (B) 3–12.75 Å^{-1}, and (C) 3–13.45 Å^{-1}.

By inspection, the observed spectral features are different both in prior to and post irradiation, and change depending on the measurement angle. This is shown more clearly for the first coordination shell around the Cu atoms in figure 11(A). Furthermore, for the irradiated sample the divergence from the pristine local structure is marked when attempting to fit the irradiated FT data to the pristine YBCO structure. The results of this fitting process are shown in figures 11(B) and (C), where for figure 11(B) the scattering paths have been constrained to correspond to the lattice parameters derived from XRD tabulated as table 1, whereas the 80° data of figure 11(C) has scattering paths where the inter atomic distances were fitted.

As figure 11(B) has the Cu-Cu distances constrained by the XRD derived lattice parameters, the respective O sites are kept in the same relative position within the YBCO unit cell. By inspection, this yields relatively good agreement between the model and the FT data, with the real component of the absorption at the bottom of each respective figure highlighting this good agreement. This indicates that most of the oxygen atoms in the *a*-*b* plane continue to occupy their expected positions between the Cu sites that define the boundaries of the *a*-*b* plane.

The 80° measurement fits plotted in figure 11(C) aim to reproduce the peak originating from the first oxygen shell around the absorbing Cu atoms, and this model does not fully

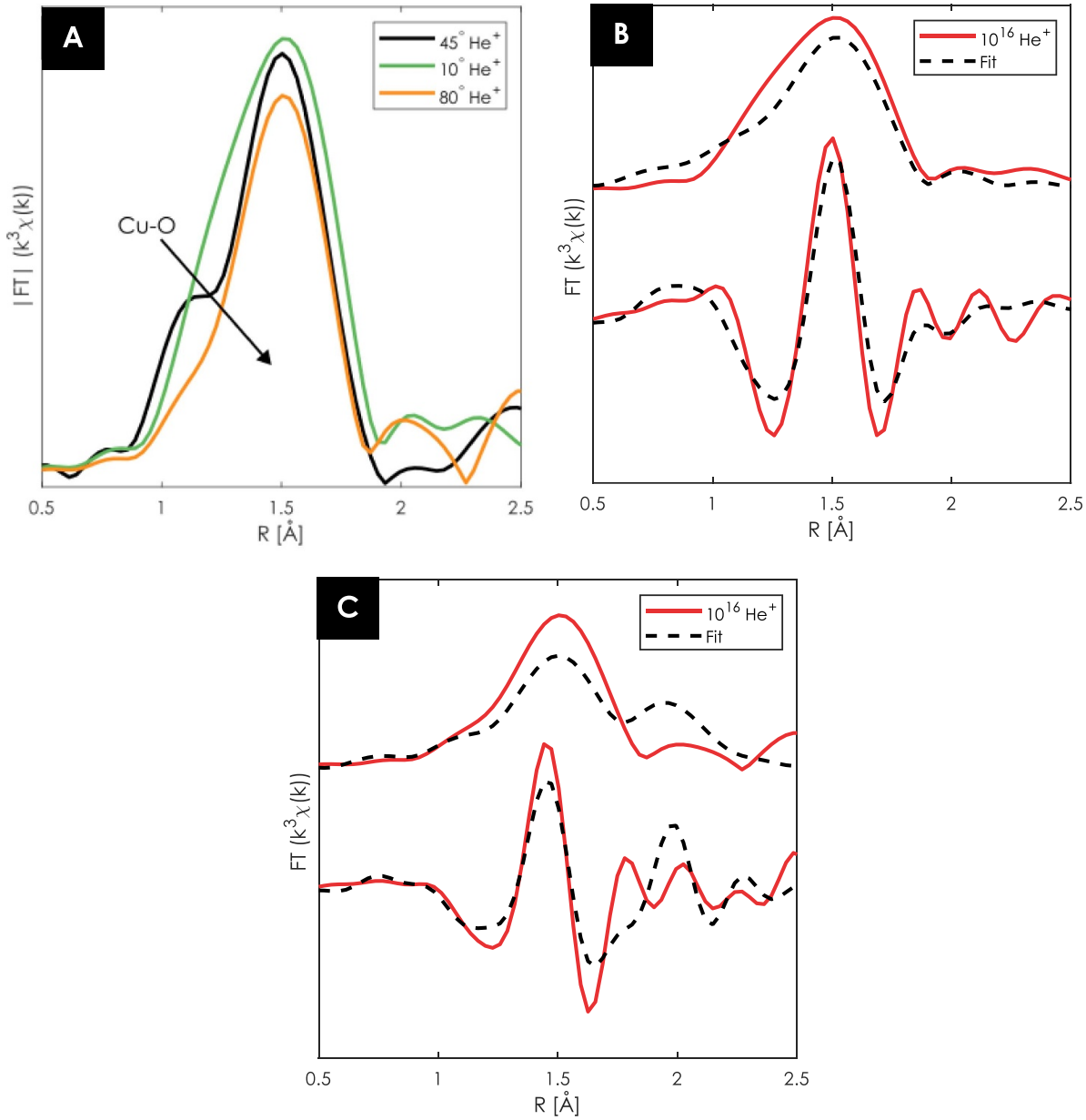

Figure 11. Analysis of irradiated sample EXAFS. (A) The magnitude of the Fourier transforms at 45° (black), 10° (green), and 80° (orange), with the main feature labelled. The other panels show experimental data (blue solid lines) and the best fit (dashed lines) of the magnitude (upper) and real part (lower) of the Fourier transform of the pristine sample EXAFS: (B) 10°, and (C) 80° measurement angles. The FT of these signals utilised k-ranges of 3–14 $Å^{-1}$ (45°), 3–12.75 $Å^{-1}$ (10°), and 3–13.45 $Å^{-1}$ (80°).

capture the shape of either the FT magnitude of the absorption spectra (at the top of the plot) or the FT real component (plotted at the base of the figure). Particularly, there is disagreement in the 1.5–2.0 Å region of figure 11(C), which corresponds to the Cu(2)-O1.1 scattering distance in the pristine REBCO structure.

3.4. Simulated EXAFS spectra

To qualitatively understand the evolution of these EXAFS data sets, modelling of the EXAFS for different unit cell structures was undertaken for comparison with the empirical data. Simulations of 45° EXAFS for REBCO-123, REBCO-124, and REBCO-123 with a Frenkel defect are plotted below in figure 12.

The simulated spectra of figure 12 are plotted relative to the pristine spectra collected from the coated conductor samples (blue) at 45°, and here it is evident that the REBCO-123 simulation (green) does not perfectly align with the experimental data. The first Cu-O shell around the 1.0–2.0 Å region is lower in amplitude and less well defined in the simulation, whereas the Cu-Ba and Cu-RE FT peak around 3.0–3.5 Å is comparatively closer in agreement to the experimental spectrum. Despite these deficiencies, the single-scattering path amplitudes occur at roughly similar inter atomic distances between the pristine experimental spectra and the simulated

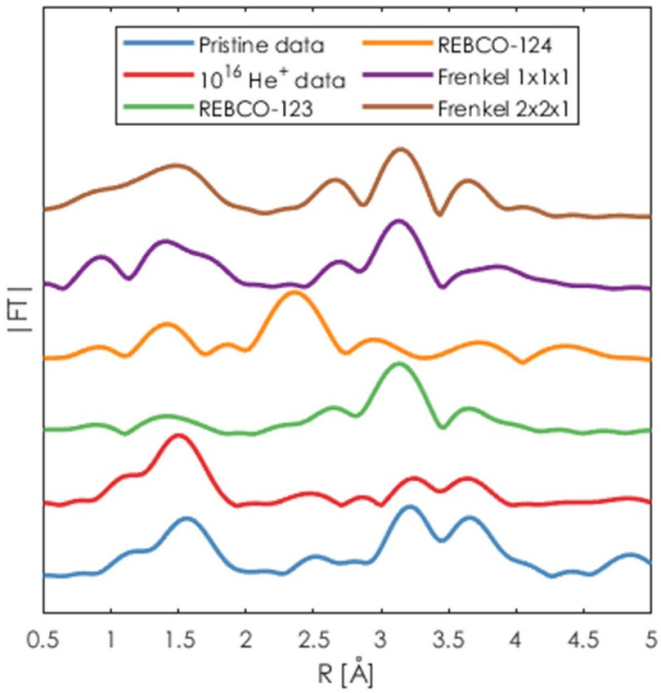

Figure 12. Comparison of the magnitude of the FT for the pristine (blue) and the irradiated (red) sample measured at 45°, and further simulated EXAFS spectra. These simulations include REBCO-123 (green), a stacking fault phase of REBCO-124 (orange), the point defect induced Frenkel defect from a 1 × 1 × 1 cell (purple), and the same defect simulated for a 2 × 2 × 1 cell (brown). The *k*-range utilised for the Fourier transforms of these simulated spectra were; 3–12.17 Å^{-1} (REBCO-123), 3–12 Å^{-1} (REBCO-124), 3–12.5 Å^{-1} (Frenkel 1 × 1 × 1), and 3–12 Å^{-1} (Frenkel 2 × 2 × 1).

REBCO-123 spectra, establishing a baseline of comparison for other simulated structures.

Notably, the REBCO-124 simulated structure has a third Cu environment, Cu(3), which is not present in the REBCO-123 structure. This introduces further Cu-O scattering path distances, which in the EXAFS FT manifest as peaks which are not possible within the REBCO-123 structure. These are most prominent in the 2.00–2.75 Å region of the FT of the REBCO-124 simulated spectra (orange), which dominate the features of this FT profile and are not observed in the experimental data. Thus, any REBCO-124 impurity or stacking faults within the pristine coated conductor appear minimal, and do not dominate the experimental spectra.

Finally, the Frenkel defect structure formed by moving an O atom at an O2 site of pristine REBCO-123, in the *a*-*b* plane between neighbouring Cu(2) atoms, to an interstitial position between two neighbouring Cu(2) atoms along the *c*-axis direction [13], are shown for two unit cell size simulations. For one of these simulations a 2 × 2 × 1 supercell was used such that 25% of the REBCO was modelled with such a defect, producing the brown spectra of figure 12. Here there is a general agreement to the observed FT of the experimental spectra post irradiation, with broader features across the range of inter atomic distance and comparable amplitudes between Cu-O dominated FT peak at low inter atomic distance and the more distant Cu-Ba, Cu-RE, and Cu-Cu FT peaks. For completeness a 1 × 1 × 1 Frenkel simulation is also included (purple), demonstrating that the pure defect case does not agree with the FT experimental 45° spectra to the same degree. This difference could arise due to the variation in the defect density within the modelled material, but could also be caused the difference in the self-interaction between defect sites in neighbouring unit cells in the 2 × 2 × 1 supercell compared to the 1 × 1 × 1 system.

4. Discussion

These measurements have established that a phase-pure, highly crystalline coated conductor of REBCO is sensitive to He$^+$ irradiation, and that the evolution of the local structure is anisotropic with respect to the REBCO unit cell. The initial quality of the pristine crystal structure was assessed by XRD measurements detailed in figures 4 and 5, and was observed to undergo the superconducting phase transition at the expected critical temperature in VSM measurements presented in figure 6.

Upon irradiation, the degradation of the crystal quality was evident both in the *c*-axis out-of-plane XRD measurements and the in-plane ω-2θ scans of figures 4 and 5 respectively, which resulted in an increase in the lattice parameters detailed in table 1, as well as a significant degradation in the superconducting transition temperature to beyond the detectable range of VSM measurements ($T_c < 10$ K). The XRD analysis indicates that the lattice expands in all directions, but with the *c*-axis increasing by a larger amount and with the a:b ratio being conserved. As such, the damage profile plotted in figure 3 was sufficient to cause the entirety of the REBCO layer of the coated conductor to lose its superconducting functionality, resulting from a significant loss of the crystalline quality.

To complement the static structure probe of the XRD characterisation of figures 4 and 5, local structure measurements using polarisation dependent Cu K-edge XAS allow the inter atomic distances around the Cu sites to be studied through the analysis of the FT of the EXAFS region. In the pristine sample measurements shown in figure 9, these were found to agree well with a $YBa_2Cu_3O_{7-\delta}$ reference structure, with the *c*-axis aligned 80° FT measurements of figure 9(C) displaying the greatest variation from this standard. From the multiple-scattering modelling, this variance is attributed to changes in the Cu-O distances along the *c*-axis, indicating a degree of inhomogeneity in O site distribution along this axis of the unit cell in the as-manufactured state. This could indicate the presence of some interstitial O atoms in the as-grown coated conductor.

Following the He$^+$ irradiation, the *a*-*b* sensitive 10° FT measurements of figure 10(B) vary minimally around the first shell peak corresponding to the Cu-O distances, indicating that the *a*-*b* plane Cu-O distances are predominantly preserved upon this irradiation treatment, and that fixing the O positions between the expanding Cu sites as determined by the XRD analysis reproduces the FT spectra well in figure 11(B). However, the 80° FT measurements plotted in figure 10(C)

show a greater degree of variation relative to the pristine spectra, with a marked increase in signal amplitude around the first Cu-O shell. This is attributed to a shift in the Cu(2)-O1.1 inter atomic distance, plotted in terms of wavenumber k in figure 7, such that the previously partially destructive interference of the Cu(1)-O1.1 and Cu(2)-O1.1 scattering paths was altered to a more constructive interference following irradiation. This would explain the observed increase in the FT amplitude in this region and would suggest that in contrast to the relative robust retention of the Cu-O distances in the *a*-*b* plane of the REBCO, the *c*-axis Cu-O distances are more susceptible to irradiation damage, indicating an anisotropic distribution of irradiation damage effects within the REBCO structure. Furthermore, the retention of the Cu-O signal indicates that the irradiation treatment does not lead to a deoxygenation of the material, consistent with our previous XANES results that showed no evidence of Cu in the $+1$ oxidation state following irradiation [13].

To further interrogate the FT experimental spectra, the simulated FT EXAFS spectra plotted in figure 12 enable a qualitative assessment of the local structure within both the pristine and irradiated coated conductor. The REBCO-124 phase does not appear to contribute to the experimental spectra, either prior to or following the irradiation treatment, and thus the stacking fault density of the manufactured material appears to be negligible. The irradiated FT data does however qualitatively agree with the simulated FT Frenkel $2 \times 2 \times 1$ spectrum, indicating that the evolution of the local structure within these samples is subtle and determined by the movement of O within the otherwise retained REBCO structure, in which the Cu, Ba and RE elements retain their relative distribution even as the unit cell of the material expands.

Whereas the model employed for fitting the pristine and irradiated REBCO FT spectra is largely focussed on the Cu-O distances present within the pristine REBCO structure, the findings of this analysis are compatible with a possible Frenkel defect, in keeping with previous studies [13]. In the analysis of figures 9 and 11, a shift in the FT peak corresponding to a *c*-axis aligned Cu-O distance is observed. In the pristine REBCO unit cell formalism, this is modelled as a shift in the Cu-O1.1 inter atomic distances, but a Frenkel defect would introduce a similar shift in the *c*-axis aligned Cu-O scattering by introducing an interstitial O site about the Cu(2) environment, such that a new *c*-axis aligned scattering path is formed. However, as the irradiation profile plotted in figure 3 is inhomogeneous due to the placement of the Bragg peak within the REBCO layer, distinguishing between a shift in the O1.1 site and the formation of Frenkel defect around the Cu(2) atom using a volume averaged local structure probe such as XAS is challenging. A validation of different defect models would be best conducted with a uniform damage profile across the REBCO layer, allowing for these subtle FT spectral shifts to be deconvoluted from the pristine structure more readily.

Whereas the exact defect structure induced by this irradiation treatment is non-trivial to determine from this data, the FT spectra indicate that the different crystallographic axes of the REBCO unit cell respond to the irradiation differently, with the *c*-axis O sites shifting more drastically than those within the *a*-*b* plane of the unit cell. This anisotropic irradiation response will inform further studies into the irradiation of REBCO coated conductors, and highlights the importance of axis specific probes in understanding the defect landscapes within these structurally complex REBCO systems.

5. Conclusion

The results of these measurements link both the degradation of crystallinity within He^+ irradiated REBCO and the loss of superconductivity within the system to changes in the local structure of the Cu atoms. Here a distinct susceptibility of the local structure to accumulated irradiation damage is seen along the *c*-axis of the material, with the *a*-*b* plane varying more subtly for the employed irradiation treatment. The evolution of the CuO scattering region of the FT spectra upon irradiation is supportive of O defect damage models within these material systems, especially given the inhomogeneous damage level and complete loss of superconductivity within these samples. This suggests that the accumulation of damage within the material is associated with O defect formation, which given the greater mobility of O, is conceivably more reversible than cation defects within the crystal lattice. These results provide further evidence of the utility of polarised EXAFS measurements in studying the defect landscape induced by irradiation in complex materials, with the employed methodology suitable for studies of other anisotropic crystal structures that are subject to irradiation.

Data availability statement

The data that support the findings of this study are openly available at the following URL/DOI: 10.5287/ora-wvdvqynd6.

Acknowledgment

R J N and S C S gratefully acknowledge financial support from the EPSRC, Grants EP/L022907/1 and EP/W011743/1 respectively. We acknowledge Diamond Light Source for access to beamline I20-Scanning under Proposal SP28846, and the Surrey Ion Beam Centre for the He^+ irradiation treatment of the samples.

ORCID iDs

Jarrod C Lewis https://orcid.org/0000-0001-7838-4241
Kirk Adams https://orcid.org/0000-0003-0179-3068
Chris R M Grovenor https://orcid.org/0000-0001-6425-354X
Rebecca J Nicholls https://orcid.org/0000-0003-3186-9772
Sofia Diaz-Moreno https://orcid.org/0000-0001-7616-6515
Susannah C Speller https://orcid.org/0000-0002-6497-5996

References

[1] Melhem Z *et al* 2015 High temperature superconducting (HTS) coils for a compact spherical Tokamak *IEEE Trans. Appl. Supercond.* **25** 1–4

[2] Sorbom B *et al* 2015 ARC: a compact, high-field, fusion nuclear science facility and demonstration power plant with demountable magnets *Fusion Eng. Des.* **100** 378–405

[3] Braccini V V *et al* 2011 Properties of recent IBAD–mocvd coated conductors relevant to their high field, low temperature magnet use *Supercond. Sci. Technol.* **24** 035001

[4] Sauerzopf F M, Wiesinger H P, Weber H W and Crabtree G W 1995 Analysis of pinning effects in $YBa_2Cu_3O_{7-\delta}$ single crystals after fast neutron irradiation *Phys. Rev.* B **51** 6002–12

[5] Chudy M *et al* 2015 n-Values of commercial YBCO tapes before and after irradiation by fast neutrons *Supercond. Sci. Technol.* **28** 035008

[6] Fischer D, Prokopec R, Emhofer J and Eisterer M 2018 The effect of fast neutron irradiation on the superconducting properties of REBCO coated conductors with and without artificial pinning centers *Supercond. Sci. Technol.* **31** 044006

[7] Unterrainer R, Fischer D, Lorenz A and Eisterer M 2022 Recovering the performance of irradiated high-temperature superconductors for use in fusion magnets *Supercond. Sci. Technol.* **35** 04LT01

[8] Prokopec R, Fischer D X, Weber H W and Eisterer M 2015 Suitability of coated conductors for fusion magnets in view of their radiation response *Supercond. Sci. Technol.* **28** 014005

[9] Iliffe W, Peng N, Brittles G, Bateman R, Webb R, Grovenor C and Speller S 2021 *In-situ* measurements of the effect of radiation damage on the superconducting properties of coated conductors *Supercond. Sci. Technol.* **34** 09LT01

[10] Iliffe W, Adams K, Peng N, Brittles G, Bateman R, Reilly A, Grovenor C and Speller S 2023 The effect of *in situ* irradiation on the superconducting performance of $REBa_2Cu_3O_{7-\delta}$-coated conductors *MRS Bull.* **48** 710–9

[11] Linden Y, Iliffe W, He G, Danaie M, Fischer D, Eisterer M, Speller S and Grovenor C 2022 Analysing neutron radiation damage in $YBa_2Cu_3O_{7-x}$ high-temperature superconductor tapes *J. Microsc.* **286** 3–12

[12] Puichaud A, Wimbush S C and Knibbe R 2017 Enhanced low-temperature critical current by reduction of stacking faults in REBCO coated conductors *Supercond. Sci. Technol.* **30** 074005

[13] Nicholls R, Diaz-Moreno S, Iliffe W, Linden Y, Mousavi T, Aramini M, Danaie M, Grovenor C and Speller S 2022 Understanding irradiation damage in high-temperature superconductors for fusion reactors using high resolution x-ray absorption spectroscopy *Commun. Mater.* **3** 52

[14] Adams K, Iliffe W, Nicholls R, He G, Diaz-Moreno S, Mosselmans F, Fischer D, Eisterer M, Grovenor C R M and Speller S C 2023 Comparing neutron and helium ion irradiation damage of $REBa_2Cu_3O_{7-\delta}$ coated conductor using x-ray absorption spectroscopy *Supercond. Sci. Technol.* **36** 10LT01

[15] Haskel D, 1998 Local structural studies of oriented high temperature superconducting cuprates by polarized XAFS spectroscopy *PhD Thesis* University Microfilms, An Arbor, MI

[16] Ziegler J F, Ziegler M D and Biersack J P 2010 SRIM—the stopping and range of ions in matter *Nucl. Instrum. Methods Phys. Res.* B **268** 1818–23

[17] MacFarlane R and Kahler A 2010 Methods for processing ENDF/B-VII with NJOY *Nucl. Data Sheets* **111** 2739–890

[18] Dennis G, Helsby W, Omar D, Horswell I, Tartoni N, Hayama S, Mikulska I and Diaz-Moreno S 2019 First results using the new DLS Xspress4 digital pulse processor with monolithic segmented HPGe detectors on XAS beamlines *Proc. 13th Int. Conf. on Synchrotron Radiation Instrumentation* vol 2054

[19] Ravel B and Newville M 2005 ATHENA, ARTEMIS, HEPHAESTUS: data analysis for x-ray absorption spectroscopy using IFEFFIT *J. Synchrotron Radiat.* **12** 537–41

[20] Beech F, Miraglia S, Santoro A and Roth R S 1987 Neutron study of the crystal structure and vacancy distribution in the superconductor $Ba_2YCu_3O_{9-\delta}$ *Phys. Rev.* B **35** 8778–81

[21] Kas J, Vila F, Pemmaraju D, Tan T S, Vimolchalao S and Rehr J 2021 Calculations of x-ray spectroscopies using FEFF10 and Corvus *J. Synchrotron Radiat.* **28** 1801–10

[22] Rehr J, Kas J, Vila F, Prange M and Jorissen K 2010 Parameter-free calculations of x-ray spectra with FEFF9 *Phys. Chem. Chem. Phys.* **12** 5503–13

[23] Clark S, Segall M, Pickard C, Hasnip P, Probert M, Refson K and Payne M 2005 First principles methods using CASTEP *Z. Kristallogr.* **220** 567–70

[24] Adachi S, Watanabe N, Seiji N, Koshizuka N and Yamauchi H 1993 Structural and superconducting properties of $(Y/Pr)Ba_2Cu_4O_8$ prepared by using O_2-HIP technique *Physica* C **207** 127–33

[25] Lomnitz M, Villarreal C and de Llano M 2013 BEC model of high-Tc superconductivity in layered cuprates *Int. J. Mod. Phys.* B **27** 1347001

[26] Chroneos A, Khadzhai G Y, Goulatis I L, Mazepulin A V, Korobkov M V and Vovk R V 2022 Effect of high pressure on temperature dependencies of the resistivty in the ab-plane of $Y_{0.77}Pr_{0.23}Ba_2Cu_3O_{7-\delta}$ *J. Mater. Sci., Mater. Electron.* **33** 9875–84

[27] Chen C, Liu L, Wen Y, Jiang Y and Chen L 2019 Elastic properties of orthorhombic $YBa_2Cu_2O_7$ under pressure *Crystals* **9** 497

[28] Kwei G H, Lawson A C, Hults W L and Smith J L 1991 Vibrational properties and atomic debye temperatures for $YBa_2Cu_3O_7$ from neutron powder diffraction *Physica* C **175** 615–22

[29] Jha R, Rani P and Awana V P S 2014 Revisiting heat capacity in bulk polycrystalline $YBa_2Cu_3O_{7-\delta}$ *J. Supercond. Nov. Magn.* **27** 287–91

[30] Lei M, Sarrao J L, Visscher W M, Bell T M, Thompson J D, Migliori A, Welp U W and Veal B W 1993 Elastic constants of a monocrystal of superconducting $YBa_2Cu_3O_{7-\delta}$ *Phys. Rev.* B **47** 61546

[31] Zemmour K, Bendjemil B and Belbah A 2013 Band structure and quantum oscillations in $YBa_2Cu_2O_7$: a local spin density approximation with the on-site Coulomb interaction study *J. Supercond. Nov. Magn.* **26** 5–19